USGS Award Number G15AP00079

Application of InSAR and modeling to investigate time-dependent seismic hazard associated with waste water injection

Manoochehr Shirzaei

Arizona State University, Tempe, Az, 85287

Phone: 4807274193

Fax: 4809658102

Duration: 05/01/2015- 04/30/2017

Abstract

The link between fluid injection and elevated seismicity on nearby fault systems has become a topic of political and scientific discussion owing to the concern that these events may eventually cause widespread damage and an overall increase in seismicity. Thus understanding the underlying physical process governing the fluid transport and that how increased fluid pressure may trigger or induce seismic event is of great importance. Here we show that wastewater injection in eastern Texas causes uplift, detectable using radar interferometric data to > 8 km from the wells. Using measured uplift, reported injection data, and a poroelastic model, we compute the crustal strain and pore pressure. We infer that a > 1 MPa increase in pore pressure in rocks with low compressibility triggers earthquakes including the Mw4.8, 17 May 2012 event, the largest earthquake recorded in east Texas. Seismic activity increased even while injection rates declined owing to diffusion of pore pressure from earlier periods with higher injection rates. Induced seismicity potential is suppressed where tight confining formations prevent pore pressure from propagating into crystalline basement rocks.

The results from this project are published in a peer reviewed journal, please see *Shirzaei et al.* [2016].

Introduction

In recent years the eastern and central USA have experienced a sharp increase in the number of earthquakes, with more than 1570 M ≥3 events between 2009 and 2015 [*Hornbach et al.*, 2015; *Rubinstein and Mahani*, 2015; *Weingarten et al.*, 2015]. Many of these events occurred near injection disposal wells and the seismicity was preceded by a high rate of fluid injection over a period of months to years, suggesting a link between seismicity and injection operations [*Frohlich et al.*, 2014; *Frohlich et al.*, 2010; *Hornbach et al.*, 2015; *Horton*, 2012; *Keranen et al.*, 2013; *Rubinstein and Mahani*, 2015; *Walsh and Zoback*, 2015]. In general, earthquake hazard is proportional to the seismic rate, thus the current increase in the seismic rate implies an elevated hazard in the central and eastern US [*Ellsworth*, 2013].

On 17 May 2012, the city of Timpson, Texas, experienced a M_w4.8 earthquake, the largest recorded event in the region (Fig. 1A). This event was preceded and followed by several earthquakes located on an inferred NW-SE trending basement fault including three with $M_w \geq$ 4.0 over the following 16 months. Focal depths were shallow, ranging from 1.6 to 5.0 km, with the majority of the strain released between 3.5 and 5 km [*Frohlich et al.*, 2014]. Four high volume Class II disposal wells are located within

~10 km and two lie directly above the earthquakes. They dispose co-produced saline formation water from oil and gas production operations in the area by injecting into Lower Cretaceous limestones within the Sabine Uplift of East Texas [*Granata*, 1963]. There are other injection wells in the vicinity, but none is closer than 7 km to the four studied wells, or is a high volume injector. The immediate area near the disposal wells or near the earthquakes has limited oil and gas production. The four disposal wells began injection between 2005 and 2007 at a net average rate of 890000 m^3/yr until mid-2012, when injection drops to 720000 m^3/yr [*Frohlich et al.*, 2014].

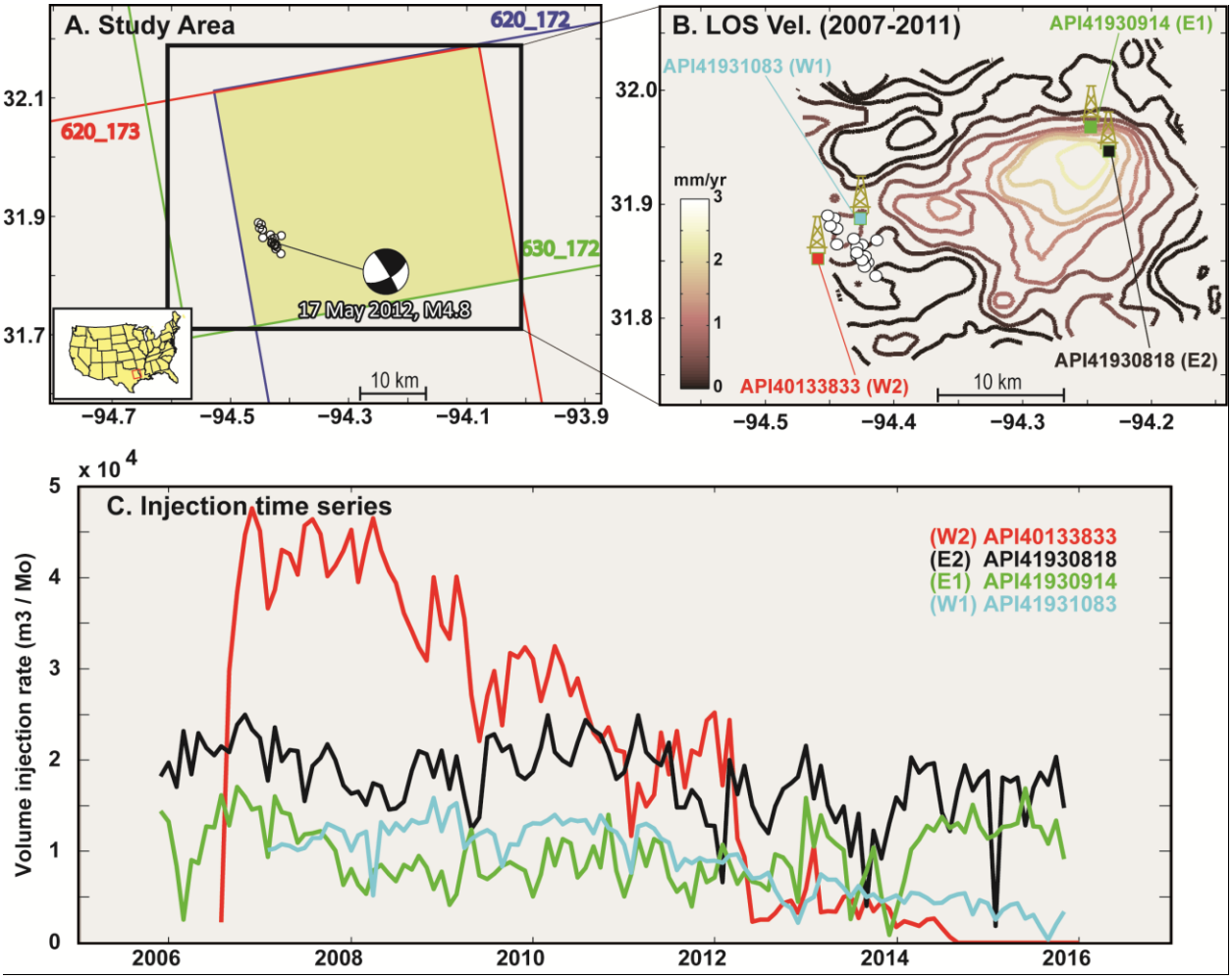

Figure 1. Study area and data sets. A. Three overlapping frames of ALOS satellite in ascending orbit (heading = 350°, incidence = 34.5°). Locations of seismicity and focal mechanism of the Timpson sequence are shown (white dots). B. LOS deformation velocity field obtained from multitemporal processing of the overlapped ALOS SAR data set. C. Time series of the volume of injected fluid for each of the wells shown in panel B. (Mo = month)

The proximity of the earthquake clusters to the injection wells suggests a link between them [*Fan et al.*, 2016; *Frohlich et al.*, 2014]. As wastewater is injected into the disposal formation, it increases pore pressure within the connected hydrologic system. Over time, the pressure perturbation can spread to distances of many km [*Hsieh and Bredehoeft*, 1981; *Keranen et al.*, 2014]. The increase in pore pressure due to the injection of fluids decreases the effective normal stress on faults, bringing them closer to failure [*Guglielmi et al.*, 2015; *Raleigh et al.*, 1976; *Zhang et al.*, 2013] as well as locally changing differential stress within the reservoir and surrounding rocks [*Chen*, 2011; *Du and Olson*, 2001; *Segall*, 1985]. Moreover, pore pressure increase can cause surface deformation [*Chen*, 2011], measurable using geodetic tools [*Vasco et al.*, 2010] and providing the possibility of documenting subsurface evolution from the surface. Among geodetic tools, interferometric synthetic aperture radar (InSAR) and Global Position System (GPS) have been widely used to monitor surface deformation due to natural and anthropogenic processes.

Methods

InSAR time series

To measure the surface deformation over the eastern Texas, we apply the Wavelet Based InSAR (WabInSAR) algorithm, a multitemporal SAR interferometric approach [*Shirzaei*, 2013; *Shirzaei and Bürgmann*, 2013]. We start with a large set of SAR images acquired from similar radar viewing geometry and then precisely coregistered them to the same master image. WabInSAR generates a large set of interferograms with respect to maximum perpendicular and temporal baselines. The flat earth effect and topography is removed using a reference digital elevation model and satellite ephemeris data [*Franceschetti and Lanari*, 1999]. The algorithm then applies a statistical framework for identifying elite (i.e. less noisy) pixels based on the complex phase noise that is estimated using wavelet analysis of the interferometric dataset. WabInSAR then implements a variety of wavelet-based filters for correcting the effects of topography correlated atmospheric delay [*Shirzaei and Bürgmann*, 2012] and orbital errors [*Shirzaei and Walter*, 2011]. Through a reweighted least square approach, WabInSAR inverts the interferometric data set and generates a uniform time series of the line-of-sight (LOS) surface deformation. The WabInSAR algorithm is thoroughly tested and validated in variety of settings for

measuring deformation associated with volcanic [*Shirzaei*, 2013] and faulting processes [*Shirzaei and Bürgmann*, 2013].

Time-dependent volume strain inversion

Here, we use a similar technique to that of *Mossop and Segall* [1999], to solve for the volume strain caused by fluid injection and associated with the observed surface deformation. To this end, the deforming volume is discretized into prism from surface to depth of 5 km. We consider a 3D array of the cuboids with 3 km × 3 km in horizontal dimensions and dz = 0.2 km in height. Within each cuboid with volume $V = dx \times dy \times dz$, the volume strain is constant and is only due to the cuboid vertical deformation. At the center of each cuboid $\{X_i, Y, Z_i\}$, we consider a horizontal Okada plane [*Okada*, 1992] buried in a homogenous isotropic elastic half-space and solve for the volume strain $u(X_i, Y, Z_i) = \frac{du_{z_i}}{dz}$, $i = 1,2,..,m$ of each cuboid, where du_z is the Okada tensile dislocation. Given the LOS surface deformation rates, $L = [L_1, L_2, \dots, L_n]^T$, we solve the following system of equations:

$$\begin{bmatrix} L_1 \\ \cdot \\ \cdot \\ \cdot \\ L_n \end{bmatrix} = [G_1 \quad \dots \quad G_m] \begin{bmatrix} u_1 \\ \cdot \\ \cdot \\ \cdot \\ u_n \end{bmatrix} + \begin{bmatrix} r_1 \\ \cdot \\ \cdot \\ \cdot \\ r_n \end{bmatrix} \quad , \; P \sim C_{ll}^{-1} \tag{1}$$

where, G includes the Okada elastic Green's functions (scaled by factor of dz) and the LOS unit vectors, $r = [r_1 \dots, r_n]^T$ is the observation residual and C_{ll} is a diagonal matrix including the variance of LOS velocities. The variance is estimated during multitemporal interferometric analysis and is on average less than 1 mm/yr [*Casu et al.*, 2006]. The variance-covariance matrix (Q) of the volume strain can be obtained as;

$$Q = \sigma_0^2 (G^T P G)^{-1} \tag{2}$$

where, σ_0^2 is the primary variance factor and usually assumed to be 1 [*Mikhail and Ackermann*, 1982]. To avoid the unrealistic variations of the volume strain, we also minimize its second derivative [*Harris and Segall*, 1987].

Poroelastic model

Taking into account the presence of a diffusing pore fluid, the concept of poroelastic theory as an extension to linear elasticity is employed [*Rice and Cleary*, 1976]. In this context the constitutive equations are:

$$2\mu\varepsilon_{ij} = \sigma_{ij} - \frac{\vartheta}{1+\vartheta}\sigma_{kk}\delta_{ij} + \frac{3(\vartheta_u - \vartheta)}{B(1+\vartheta)(1+\vartheta_u)} p\delta_{ij} \tag{3}$$

$$m - m_0 = \frac{3\rho_0(\vartheta_u - \vartheta)}{3\mu B(1+\vartheta)(1+\vartheta)} [\sigma_{kk} + \frac{3}{B} p] \tag{4}$$

where, p is the excess pore pressure, σ_{ij} is total stresses, μ and ϑ are the shear modulus and Poisson's ratio when the material is deformed under drained conditions, $\vartheta \leq \vartheta_u \leq 0.5$, B is the bulk modulus and m_0 is the mass at reference state. Equation (3) is derived from equilibrium conditions and Equation (4) presents the conservation of the water mass by applying Darcy's law to fluid flow in the pore space.

Wang and Kumpel [2003] presented a numerical solution to obtain surface displacement and pore pressure due to forcing fluid through a point source, such as fluid injection in a multilayered half-space. Here we adapt their approach to model the distribution of pore pressure due to the fluid injection.

Results and Discussions

We applied the multitemporal InSAR approach [*Shirzaei*, 2013] to three overlapping sets of L-band SAR images acquired by ALOS satellite over the Timpson area during 2007/05/06 and 2010/11/14 (Fig. 1A). High quality interferograms were generated from this L-band data. We improved the signal-to-noise-ratio of the measurements by estimating the linear velocity from time series obtained from inverting a large number of interferograms . We find up to 3 mm/yr of uplift in line-of-sight (LOS) over the area between the injection wells (Fig. 1B) from velocity maps obtained for each individual data set and the combined map. We estimated that the rate of volume increase under the LOS velocity surface is $800000 - 1000000$ m^3/yr, assuming an elastic material with a Poisson's ratio of 0.25 - 0.33 estimated from seismic velocities profiles, consistent with the net injected volume rate at the injection wells.

The two western wells (W1 and W2) inject (Fig. 1C) at a depth of 1800 m into Trinity Group formations, a porous and permeable limestone that is overlain by the regionally-extensive and much less permeable Ferry Lake Anhydrite [*Granata*, 1963]. The east wells (E1 and E2) inject (Fig. 1C) into carbonate formations of the Washita Group at a depth of 900 m, stratigraphically above the Ferry Lake Anhydrite [*Granata*, 1963]. The pressure change due to injection is the likely cause of the surface uplift. We applied an inverse modeling scheme [*Mossop and Segall*, 1999] to characterize the rate of volume strain. We discretized the volume beneath the half space into rectangular prisms, 3×3 km in area by 0.2 km high between the surface and a depth of 5 km. We assumed constant volume strain within each prism . Our optimum strain model accurately reproduces the observed deformation data and has a total volume change of 700000 ± 1600 m^3/yr, slightly lower than the injection rate. This

discrepancy is likely due to diffusion of injected fluids into the surrounding rocks without generating any measureable deformation. We also found a maximum volume strain rate of ~1.5×10^{-6} yr^{-1}, at a depth of 0.8 - 1.1 km adjacent to wells E1 and E2 (Fig. 2A).

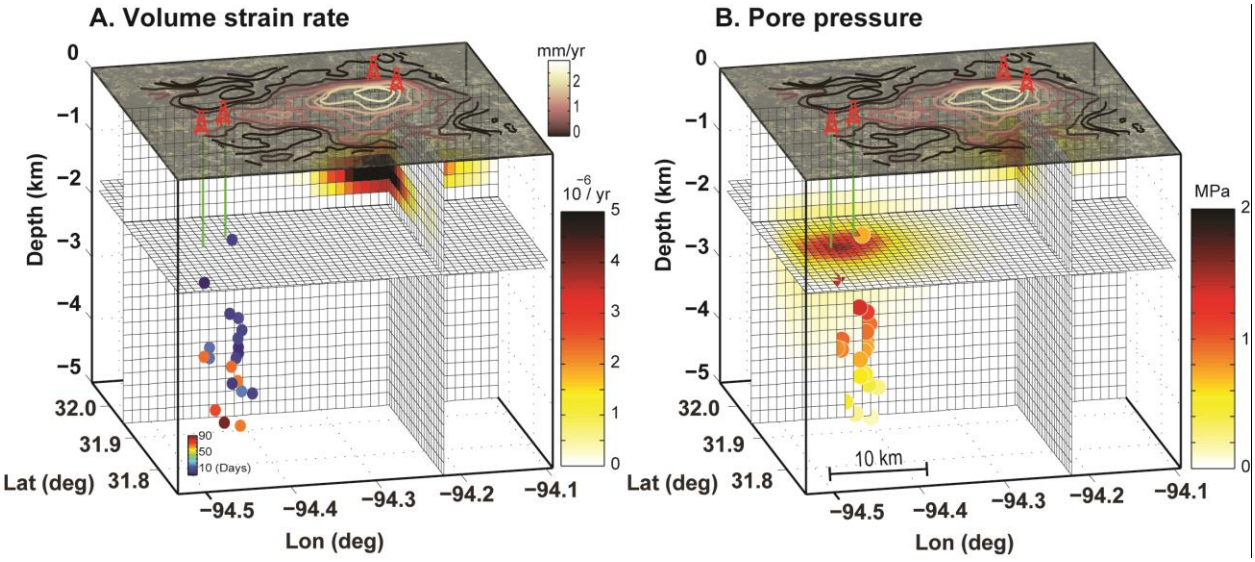

Figure 2. Volumetric strain and pore pressure. A. Distribution of the estimated volume strain rate. Colored circles show the timing of earthquakes with respect to the first event. The injection wells are also shown by green bars. Contour lines show the surface deformation rate between 2007/05/06 and 2010/11/14. B. Distribution of the cumulative pore pressure between 2006 and 2013. Colored circles show the pore pressure increase at the location of earthquakes.

The availability of geological profiles and distribution of hydraulic conductivity and Poisson's ratios, allowed us to characterize parameters of a poroelastic layered Earth model. Using this Earth model and the time series of injected fluid volume, we solve for the evolution of the pore pressure in the crust (Fig. 2B). We identified two zones of maximum pore pressure at depths of ~0.85 km and ~1.85 km depth near east and west wells, respectively. The shallower zone of elevated pore pressure also coincides with the zone of maximum volume strain. Higher pressures occur around the two west wells where uplift was negligible. The contribution from other injection wells to the south is small and of second-order importance. The pore pressure associated with wells to the north is unlikely to influence the seismicity as they lie north and on the downthrown block of the Mount Enterprise fault system [*Granata*, 1963], which likely acts as a barrier to southward migration of the fluids.

To investigate the relationship between pore pressure distribution associated with injection and the observed seismicity, we estimate the pore pressure increase at the location of the 2012 seismic events, where the main events nucleated between 3.5 and 4.5 km depth [*Frohlich et al.*, 2014]. Overall, fluid injection caused a pore pressure increase of 0.5-1.5 MPa at the hypocentral depth. Pressure changes of this magnitude trigger earthquakes elsewhere [*Roeloffs*, 1996]. In the context of Mohr circle stress analysis, a localized increase in pore pressure shifts the circle to the left (i.e., reduces the effective normal stress) and changes its radius because of poroelastic strain (i.e., increases the differential stress), while a spatially uniform pore pressure increase only shifts the circle to the left until it touches the failure envelope [*Rozhko et al.*, 2007]. Given the lack of historical large earthquakes in the region and the five year delay between the initiation of injection and the first large event, we suggest that a decrease in effective normal stress (due to a homogeneous increase in pore pressure) triggered seismicity. The second condition is only satisfied when the pore pressure increase is localized. The initiating seismicity and associated stress change potentially enhanced the permeability transiently [*Brodsky et al.*, 2003; *Kitagawa et al.*, 2002; *Roeloffs*, 1988; *Rojstaczer and Wolf*, 1992], increasing the pore pressure at the location of the deeper events, which in turn promoted further earthquakes.

We investigated injection from two pairs of wells that began injecting at approximately the same time, disposing approximately the same volumes of wastewater. The main differences are depth of injection and the presence of an impermeable barrier below the shallower east wells that blocks fluid and pressure from reaching deeper formations. The deeper west wells are associated with the 2012 Timpson earthquake sequence, while no detected seismicity occurred near the east wells. This observation highlights the importance of hydrogeology for the consequences of fluid injection.

The extent to which induced pore pressure change occurs, it is an important parameter to accurately estimate seismic hazard. From a regulatory perspective, however, constraining this parameter is not trivial due to its complex relationship with local hydrogeology [*Shapiro et al.*, 1999]. Using deformation data we are able to put a lower bound on the extent of the rock volume change caused by pore pressure increase. Measurable uplift more than 8 km from the east wells demonstrates the long reach of pressure perturbations inferred in other studies [*Hsieh and Bredehoeft*, 1981; *Keranen et al.*, 2014; *Zhang et al.*, 2013].

Studies of potentially induced earthquakes suggest that the majority of seismicity occurs within basement rocks, even though most of the injection is done in more shallow sedimentary layers [*Frohlich*

et al., 2014; *Hornbach et al.*, 2015; *Horton*, 2012; *Keranen et al.*, 2013; *Nicholson et al.*, 1988; *Seeber et al.*, 2004; *Weingarten et al.*, 2015]. While pore pressure has increased adjacent to both of the east and west wells, little surface deformation was detected in the vicinity of the west wells, where the seismicity occurred (Fig. 2). This observation is likely due to lower rock compressibility near west wells compared to that of east wells, a feature we did not account for in solving for the pore pressure evolution, in addition to the greater injection depth. Moreover, injection in the east wells is done in a shallow layer, typically characterized by velocity strengthening frictional properties [*Scholz*, 2002], thus pore pressure changes are less likely to initiate seismic rupture. The uplift signal also has an asymmetric pattern, which we cannot explain with standard models of radial pore pressure diffusion in a homogenous medium. Our model shows that pore pressure propagates downward below the west wells with delay and that the period of elevated seismicity between 2010 and 2014 coincides with the period of maximum pore pressure change of 1-2.5 MPa at the average depth of 3 km (Fig. 3A). Though all events coincide with the period of pore pressure increase in the focal zone, the onset of the main sequence in May 2012 corresponds to pressures of about 1 MPa reaching the focal zone (Fig. 3B).

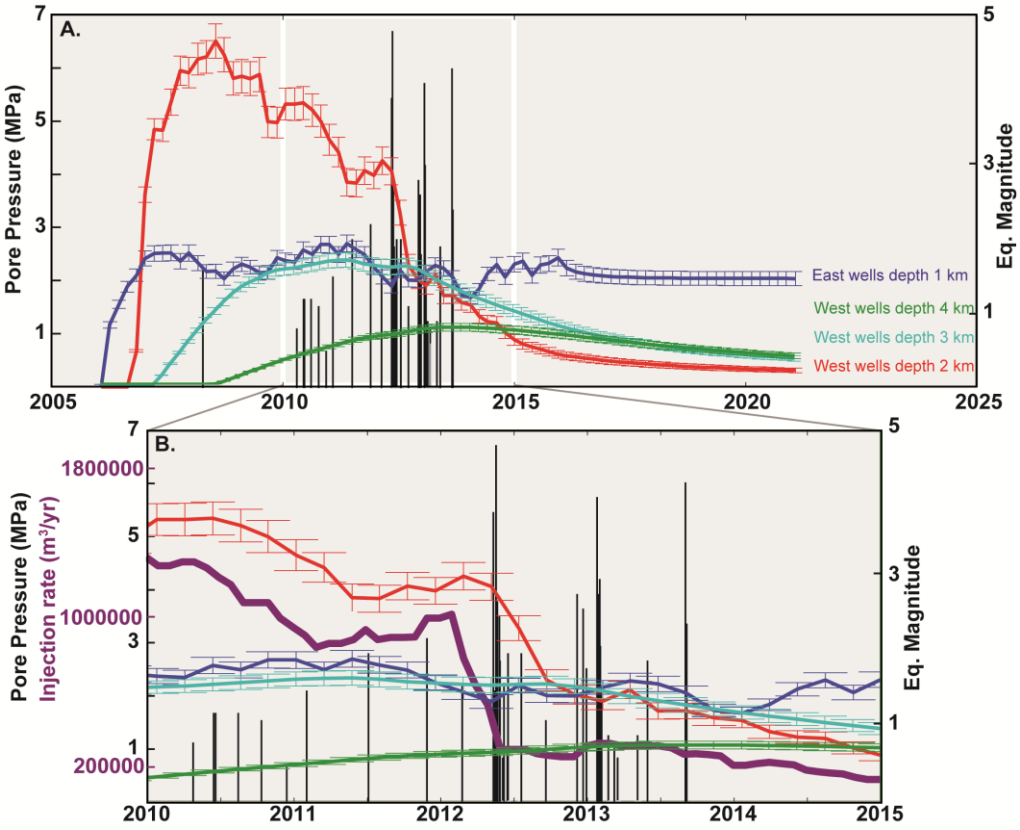

Figure 3. Pore pressure time series. A. Colored lines show time series of pore pressure at various depths. The errorbars show one standard deviation uncertainty and are obtained through bootstrapping. Vertical black lines show the time and magnitude of earthquakes in the Timpson sequence (Table S7). B. Zoom of the period 2010-2015 from panel A. The time series of the total injected fluid at west wells is superimposed in purple.

The frequency and magnitude of events reached a climax between May 2012 and September 2013, when more than 80% of events occurred, including four M_w4+ earthquakes. This period of elevated seismic activity follows a rapid decline in injection at the west wells (Fig. 3B). Thus, the timing of seismicity may result from pore pressure diffusion to the depths of the earthquakes. Additional contributions to the stresses may also promote seismicity from the poroelastic stresses near the well that accompany the decrease in injection. For an optimally oriented strike-slip fault with fault-normal radial to the injection site, a sudden decline in injection rate relaxes the compressive stress [*Segall and Lu*, 2015]. All of the seismic events here occurred on a fault with fault-normal oriented at N60°E radial to the west injection wells.

Our coupled flow and poroelastic model allows us to predict the future pore pressure distribution after injection ends (Fig. 3A). We notice that as injection ends in west wells by about 2016, the pressure decreases approximately exponentially. However, the decay rate is fastest in the most permeable formations and at the depths where injection occurs. At the east wells, 10 years after shut off, the pore pressure remains close its maximum level. For the west wells, only 5 years after a hypothesized shut off pore pressure drops to the less than 10% of its maximum value. This observation has direct implication for future injection operations and seismic hazard. Changes in the seismicity rate is a function of changes in Coulomb stress and background stress [*Dieterich*, 1994]. Our study shows the background stress is characterized by a relaxation time that depends on both the injection history and hydrogeological properties. Therefore, injection history at a given site may modify future estimates of the seismic hazard.

Better quantification of the evolution of the stress and pore pressure in the crust is vital to forecast fault reactivation [*Ellsworth*, 2013; *McClure and Horne*, 2011]. Despite improvements to seismic monitoring capacity and the resulting decrease in the magnitude detection threshold [*Deichmann and Giardini*, 2009; *Kim*, 2013], observations of the in-situ pore pressure and stress field remain elusive due

to scarcity of deformation observations and integration of observations with physical models. This work highlights the value of monitoring surface deformation, in particular using advanced remote sensing techniques, to understand the evolution of pore pressure and stress at depth. The ability to measure crustal stress evolution presents a proactive approach to managing hazard associated with fluid injection. Observation of the time-dependent stress field permits the construction of temporally variable statistical frameworks [*Segall and Lu*, 2015], which are useful for earthquake operational forecasting [*Jordan et al.*, 2011]. The key to successful operational earthquake hazard assessment is being able to continuously update information about the probability of a future earthquake, which can be achieved using data and models such as those presented in this study. Geodetic monitoring and modeling schemes are valuable components for induced seismic hazard mitigation efforts.

References

Materials and Methods are available as supplementary materials on Science Online.

Brodsky, E. E., E. Roeloffs, D. Woodcock, I. Gall, and M. Manga (2003), A mechanism for sustained groundwater pressure changes induced by distant earthquakes, *J. Geophys. Res.*, *108*(B8), doi:doi: 10.1029/2002JB002321.

Casu, F., M. Manzo, and R. Lanari (2006), A quantitative assessment of the SBAS algorithm performance for surface deformation retrieval from DInSAR data, *Remote Sensing of Environment*, *102*(3), 195-210.

Chen, Z. R. (2011), Poroelastic model for induced stresses and deformations in hydrocarbon and geothermal reservoirs, *Journal of Petroleum Science and Engineering*, *80*(1), 41-52, doi:10.1016/j.petrol.2011.10.004.

Deichmann, N., and D. Giardini (2009), Earthquakes Induced by the Stimulation of an Enhanced Geothermal System below Basel (Switzerland), *Seismological Research Letters*, *80*(5), 784-798, doi:10.1785/gssrl.80.5.784.

Dieterich, J. H. (1994), A constitutive law for rate of earthquake production and its application to earthquake clustering, *J. Geophys. Res.*, *99*, 2601-2618.

Du, J., and J. E. Olson (2001), A poroelastic reservoir model for predicting subsidence and mapping subsurface pressure fronts, *Journal of Petroleum Science and Engineering*, *30*(3-4), 181-197, doi:10.1016/s0920-4105(01)00131-0.

Ellsworth, W. L. (2013), Injection-Induced Earthquakes, *Science 341*, doi:10.1126/science.1225942.

Fan, Z., P. Eichhubl, and J. F. Gale (2016), Geomechanical analysis of fluid injection and seismic fault slip for the Mw4. 8 Timpson, Texas, earthquake sequence, *Journal of Geophysical Research: Solid Earth*, *121*(4), 2798-2812.

Franceschetti, G., and R. Lanari (1999), *Synthetic aperture radar processing*, CRC Press.

Frohlich, C., W. Ellsworth, W. A. Brown, M. Brunt, J. Luetgert, T. MacDonald, and S. Walter (2014), The 17 May 2012 M4.8 earthquake near Timpson, East Texas: An event possibly triggered by fluid injection, *Journal of Geophysical Research: Solid Earth*, *119*(1), 581-593, doi:10.1002/2013jb010755.

Frohlich, C., E. Potter, C. Hayward, and B. Stump (2010), Dallas-Fort Worth earthquakes coincident with activity associated with natural gas production, *The Leading Edge*, 0 - 5.

Granata, W. H. (1963), Cretaceous stratigraphy and structural development of the Sabine Uplift area, Texas and Louisiana.*Rep.*, Shreveport Geological Society.

Guglielmi, Y., F. Cappa, J.-P. Avouac, P. Henry, and D. Elsworth (2015), Seismicity triggered by fluid injection-induced aseismic slip, *Science*, *348*(6240), 1224-1226, doi:10.1126/science.aab0476.

Harris, R., and P. Segall (1987), Detection of a locked zone at depth on the Parkfield, California segment of the San Andreas fault, *J. Geophys. Res.*, *92*, 7945-7962.

Hornbach, M. J., H. R. DeShon, W. L. Ellsworth, B. W. Stump, C. Hayward, C. Frohlich, H. R. Oldham, J. E. Olson, M. B. Magnani, and C. Brokaw (2015), Causal factors for seismicity near Azle, Texas, *Nature communications*, *6*.

Horton, S. (2012), Disposal of Hydrofracking Waste Fluid by Injection into Subsurface Aquifers Triggers Earthquake Swarm in Central Arkansas with Potential for Damaging Earthquake, *Seismological Research Letters*, *83*(2), 250-260, doi:10.1785/gssrl.83.2.250.

Hsieh, P. A., and J. D. Bredehoeft (1981), A reservoir analysis of the Denver earthquakes: A case of induced seismicity., *Journal of Geophysical Research*, *86*(NB2), 903-920, doi:10.1029/JB086iB02p00903.

Jordan, T. H., Y.-T. Chen, P. Gasparini, R. Madariaga, I. Main, W. Marzocchi, G. Papadopoulos, G. Sobolev, K. Yamaoka, and J. Zschau (2011), Operational Earthquake Forecasting: State of Knowledge and Guidelines for Utilization, *Annals of Geophysics*, *54*(4), 315-391.

Keranen, K. M., H. M. Savage, G. A. Abers, and E. S. Cochran (2013), Potentially induced earthquakes in Oklahoma, USA: Links between wastewater injection and the 2011 Mw 5.7 earthquake sequence, *Geology*, *41*(6), 699-702, doi:10.1130/g34045.1.

Keranen, K. M., M. Weingarten, G. A. Abers, B. A. Bekins, and S. Ge (2014), Sharp increase in central Oklahoma seismicity since 2008 induced by massive wastewater injection, *Science*, *345*(6195), 448-451, doi:10.1126/science.1255802.

Kim, W.-Y. (2013), Induced seismicity associated with fluid injection into a deep well in Youngstown, Ohio, *Journal of Geophysical Research: Solid Earth*, *118*(7), 3506-3518, doi:10.1002/jgrb.50247.

Kitagawa, Y., K. Fujimori, and N. Koizumi (2002), Temporal change in permeability of the rock estimated from repeated water injection experiments near the Nojima fault in Awaji Island, Japan, *Geophysical Research Letters*, *29*(10), doi:10.1029/2001gl014030.

McClure, M. W., and R. N. Horne (2011), Pressure Transient Analysis of Fracture Zone Permeability at Soultz-sous-Forêts, *GRC Transactions*, *35*.

Mikhail, E. M., and F. E. Ackermann (1982), *Observations and least squares*, University Press of America.

Mossop, A., and P. Segall (1999), Volume strain within The Geysers geothermal field, *Journal of Geophysical Research-Solid Earth*, *104*(B12), 29113-29131, doi:Doi 10.1029/1999jb900284.

Nicholson, C., E. Roeloffs, and R. L. Wesson (1988), The northeastern Ohio earthquake of 31 January 1986: Was it induced?, *Bull. Seism. Soc. Am.*, *78*, 188-217.

Okada, Y. (1992), Internal deformation due to shear and tensile faults in a half-space, *Bull. Seism. Soc. Am.*, *82*, 1018-1040.

Raleigh, C. B., J. H. Healy, and J. D. Bredehoeft (1976), An Experiment in Earthquake Control at Rangely, Colorado, *191*(4233), 1230-1237 doi:DOI: 10.1126/science.191.4233.1230.

Rice, J. R., and M. P. Cleary (1976), Some basic stress diffusion solutions for fluid-saturated elastic porous media with compressible constituents, *Rev. Geophys. Space Phys.*, *14*, 227-241.

Roeloffs, E. A. (1988), Hydrologie precursors to earthquakes: A review, *Pageoph*, *126*, 177-210.

Roeloffs, E. A. (1996), Poroelastic methods in the study of earthquake-related hydrologic phenomena, in *Advances in Geophysics*, edited by R. Dmowska, Academic Press, San Diego.

Rojstaczer, S., and S. Wolf (1992), Permeability changes associated with large earthquakes: An example from Loma Prieta, California., *Geology*, *20*(3), 211-214, doi:10.1130/0091-7613(1992)020<0211:pcawle>2.3.co;2.

Rozhko, A. Y., Y. Y. Podladchikov, and F. Renard (2007), Failure patterns caused by localized rise in pore-fluid overpressure and effective strength of rocks, *Geophysical Research Letters*, *34*(22), doi:10.1029/2007gl031696.

Rubinstein, J. L., and A. B. Mahani (2015), Myths and Facts on Wastewater Injection, Hydraulic Fracturing, Enhanced Oil Recovery, and Induced Seismicity, *Seismological Research Letters*, *86*(4), 1060-1067, doi:10.1785/0220150067.

Scholz, C. H. (2002), *The Mechanics of Earthquakes and Faulting*, Cambridge Univ. Press, Cambridge, 2nd. ed. 496 pp.

Seeber, L., J. G. Armbruster, and W.-Y. Kim (2004), A fluid-injection-triggered earthquake sequence in Ashtabula, Ohio: implications for seismogenesis in stable continental regions, *Bulletin of the Seismological Society of America*, *94*(1), 76-87.

Segall, P. (1985), Stress and Subsidence Resulting from Subsurface Fluid Withdrawal in the Epicentral Region of the 1983 Coalinga Earthquake, *Journal of Geophysical Research-Solid Earth and Planets*, *90*(Nb8), 6801-6816, doi:Doi 10.1029/Jb090ib08p06801.

Segall, P., and S. Lu (2015), Injection-induced seismicity: Poroelastic and earthquake nucleation effects, *Journal of Geophysical Research-Solid Earth*, *120*(7), 5082-5103, doi:10.1002/2015jb012060.

Shapiro, S. A., P. Audigane, and J.-J. Royer (1999), Large-scale in situ permeability tensor of rocks from induced microseismicity, *Geophys. J. Int.*, *137*(1), 207-213.

Shirzaei, M. (2013), A Wavelet-Based Multitemporal DInSAR Algorithm for Monitoring Ground Surface Motion, *Ieee Geoscience and Remote Sensing Letters*, *10*(3), 456-460, doi:Doi 10.1109/Lgrs.2012.2208935.

Shirzaei, M., and R. Bürgmann (2012), Topography correlated atmospheric delay correction in radar interferometry using wavelet transforms, *Geophysical Research Letters*, *39*(1), doi: 10.1029/2011GL049971.

Shirzaei, M., and R. Bürgmann (2013), Time-dependent model of creep on Hayward fault inferred from joint inversion of 18 years InSAR time series and surface creep data, *J. Geophys. Res. Solid Earth*, *118*(1733–1746), doi:10.1002/jgrb.50149.

Shirzaei, M., W. L. Ellsworth, K. F. Tiampo, P. J. González, and M. Manga (2016), Surface uplift and time-dependent seismic hazard due to fluid injection in eastern Texas, *Science*, *353*(6306), 1416-1419, doi:10.1126/science.aag0262.

Shirzaei, M., and T. R. Walter (2011), Estimating the Effect of Satellite Orbital Error Using Wavelet-Based Robust Regression Applied to InSAR Deformation Data, *Ieee Transactions on Geoscience and Remote Sensing*, *49*(11), 4600-4605, doi:Doi 10.1109/Tgrs.2011.2143419.

Vasco, D. W., A. Rucci, A. Ferretti, F. Novali, R. C. Bissell, P. S. Ringrose, A. S. Mathieson, and I. W. Wright (2010), Satellite-based measurements of surface deformation reveal fluid flow associated with the geological storage of carbon dioxide, *Geophysical Research Letters*, *37*, doi:10.1029/2009gl041544.

Walsh, F. R., and M. D. Zoback (2015), Oklahoma's recent earthquakes and saltwater disposal, *Science advances*, *1*(5), e1500195.

Wang, R. J., and H. J. Kumpel (2003), Poroelasticity: Efficient modeling of strongly coupled, slow deformation processes in a multilayered half-space, *Geophysics*, *68*(2), 705-717, doi:10.1190/1.1567241.

Weingarten, M., S. Ge, J. W. Godt, B. A. Bekins, and J. L. Rubinstein (2015), High-rate injection is associated with the increase in US mid-continent seismicity, *Science*, *348*(6241), 1336-1340, doi:10.1126/science.aab1345.

Zhang, Y., M. Person, J. Rupp, K. Ellett, M. A. Celia, C. W. Gable, B. Bowen, J. Evans, K. Bandilla, P. Mozley, T. Dewers, and T. Elliot (2013), Hydrogeologic Controls on Induced Seismicity inCrystalline Basement Rocks Due to Fluid Injection into Basal Reservoirs, *Ground Water*, *51*(4), 525-538, doi:10.1111/gwat.12071.